

A molecular beam apparatus for eigenstate-resolved studies of gas-surface reactivity

P. R. McCabe, L. B. F. Juurlink, and A. L. Utz

Department of Chemistry and W. M. Keck Foundation Laboratory for Materials Chemistry, Tufts University, Medford, Massachusetts 02155

(Received 10 August 1999; accepted for publication 15 September 1999)

A new supersonic molecular beam-surface scattering apparatus permits eigenstate-resolved measurements of gas-surface reactivity. Infrared light from a narrow-bandwidth tunable laser intersects a supersonic molecular beam and prepares an ensemble of molecules in a single rotational and vibrational quantum state. The energized molecules, with their well-defined translational, vibrational, and rotational energies, pass into an ultrahigh vacuum chamber and impinge on a single crystal metal surface where their reactivity is quantified. The apparatus provides independent control over translational, vibrational, and rotational degrees of freedom and permits highly detailed studies of gas-surface reactivity. In this article we describe the design and characterization of our apparatus and illustrate its use to study the dissociative chemisorption of methane on Ni(100). © 2000 American Institute of Physics. [S0034-6748(00)00701-2]

I. INTRODUCTION

Measuring the reactivity of molecules in selected quantum states has been a goal of surface scientists for many years.^{1,2} Such studies provide highly detailed data that test theories, reveal the origin of activation barriers to gas-surface reactivity, and identify the most reactive species in a thermal distribution of molecules. Despite many attempts, quantum-state-resolved results for neutral molecules with a well-defined translational energy have only recently become available for several diatom-surface systems.^{3,4} Our direct measurements of state-resolved sticking probabilities for methane dissociation on Ni(100) are the first such results for a polyatomic molecule in a beam-surface study, and they represent an important step toward studying increasingly complex systems.⁵ This report describes in detail the experimental apparatus we have used to make those measurements.

The energy of a gas-phase reagent can play a major role in direct dissociative chemisorption, where incident molecules dissociate and the resulting molecular fragments chemisorb upon impact with a surface.⁶ Identifying the molecular motions most efficient at promoting reactivity reveals the nature of the reaction coordinate in the region of the transition state and provides crucial insight into the molecular-level mechanism for the reaction. Identifying those coordinates, though, presents a formidable experimental challenge. The potential energy surface governing the process is characterized by many degrees of freedom that include the translational, rotational, and vibrational motion of the incident molecule and its orientation and angle of incidence on the surface. Polyatomic reagents have many (3N-6) vibrational modes, and a particular eigenstate of the molecule may involve simultaneous excitation along two or more of these coordinates, further increasing the number of unique internal motions available to the incident molecule. Experiments using thermal samples of molecules provide reaction probabilities averaged over the entire internal state

distribution present in the thermal sample. In all but the sparsest of systems (H₂), such averaging prevents an unambiguous identification of the most reactive coordinates.⁷⁻⁹

A number of research groups have coupled a supersonic molecular beam source with an ultrahigh vacuum surface analysis chamber to eliminate much of the thermal averaging over translational degrees of freedom for the incident molecule.¹⁰⁻¹² Cooling during the supersonic expansion generally results in a significant narrowing of the translational energy and rotational state distribution of molecules incident on the surface, but generally does little to alter the thermal distribution of vibrational states of molecules in the beam.^{13,14} An additional advantage of the beam-surface approach is that it provides independent control over the chemical composition, structure, and temperature of the surface, all of which may influence reactivity.

We have recently built and characterized an experimental apparatus that extends the versatility of a conventional supersonic molecular beam-surface machine by adding eigenstate-selective infrared excitation of molecules in the beam with a high resolution, continuous wave (cw), single-mode infrared laser. Infrared excitation prepares a significant population of gas phase reagent molecules in a single rotational and vibrational quantum state while the supersonic molecular beam controls the molecules' translational energy and angle of incidence on the surface. Therefore, our approach specifies all energetic degrees of freedom in the incident molecule as well as the character of its vibrational excitation. Detecting the surface-bound reaction products with Auger electron spectroscopy offers a sensitive and direct probe of the state-selected molecules' reactivity.

The properties of the infrared light we generate, the supersonic molecular beam, and the molecules we study allow us to excite single quantum states selectively. After the initial stages of the expansion, the molecules in the beam suffer very few collisions, and the natural lifetime for radiative de-

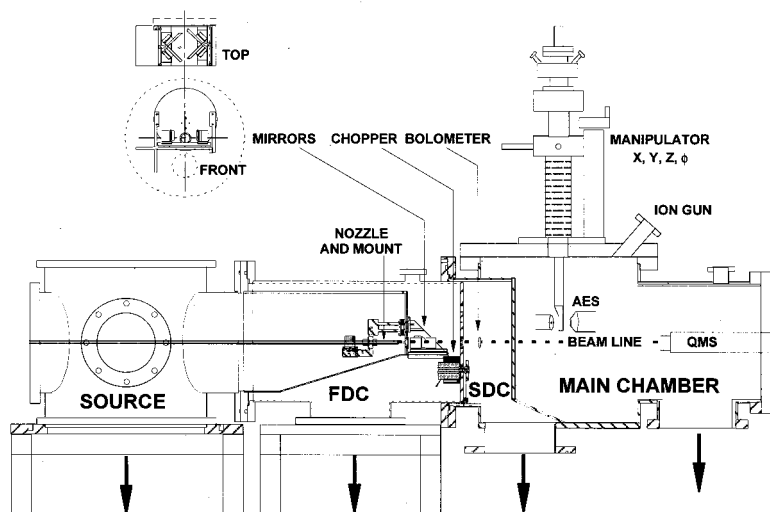


FIG. 1. Molecular beam-surface analysis chamber showing the four vacuum chambers, the source, first differential pumping stage (FDC), second differential pumping stage (SDC), and main surface analysis chamber. The drawing is to scale.

cay of vibrational eigenstates exceeds 10 ms.^{15,16} These two factors result in very sharp absorption profiles for the molecules in the beam. Rotational cooling in the beam greatly reduces rotational congestion in the absorption spectrum, and in diatomic and small polyatomic molecules, the density of vibrational states is sufficiently low that the transitions we excite are well resolved. In the absence of overlapping transitions, our high-resolution laser excites molecules to a single rovibrational eigenstate with a constant and well-defined vibrational character. Intramolecular vibrational redistribution (IVR), in which the vibrational character of the prepared state evolves in time, can only occur when two or more eigenstates are coherently excited by the laser radiation. Since we excite single eigenstates, the states we prepare do not exhibit IVR.

In addition to being selective, our approach efficiently excites many molecules to the target quantum state. The high spectral brightness of the laser source, coupled with the sharp absorption profile for molecules in the molecular beam, results in high excitation efficiencies that, under favorable conditions, can approach saturation of the optical transition. Since the cw laser irradiates molecules continuously, this high excitation efficiency applies to the entire flux of molecules incident on the surface. For experiments such as ours, where we probe dissociative chemisorption directly by de-

tecting the adsorbed reaction products, this feature minimizes interference due to adsorption of less reactive, but more abundant molecules that are not excited by the laser.

The remainder of this report details our experimental apparatus and its performance. We first describe our beam-surface apparatus, including the characterization of our molecular beam, which controls the translational energy of molecules incident on the surface. Next, we document the optical system that creates the ensemble of state-selected molecules and explain how we determine the flux of state-selected molecules incident on the surface. We then outline our technique for detecting the reaction products and conclude with an example of an eigenstate-resolved measurement of methane dissociation on Ni(100).

II. MOLECULAR BEAM APPARATUS

A. Chamber design

The design of our triply differentially pumped supersonic molecular beam-surface analysis chamber is based on that of other groups,¹¹ but includes additional features to permit the excitation and detection of state-selected molecules in the beam. Figure 1 depicts the key features of our apparatus, and Fig. 2 provides critical dimensions along the

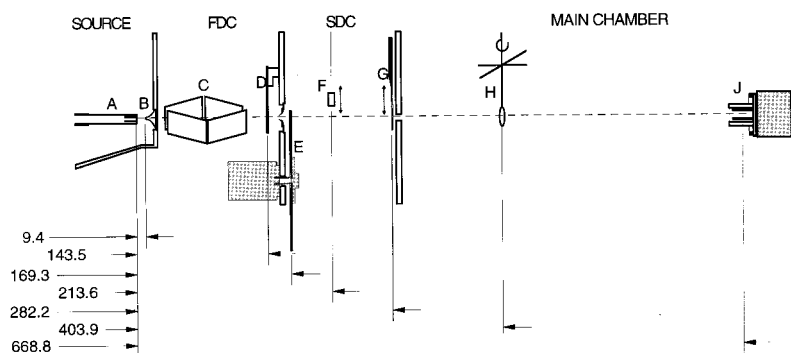


FIG. 2. Key dimensions, in mm, and locations of the (A) nozzle, (B) skimmer, (C) multipass cell, (D) shutter, (E) chopper blade, (F) pyroelectric bolometer, (G) sliding beam valve, (H) Ni(100) crystal, and (J) center of the mass spectrometer ionizer assembly.

TABLE I. Vacuum system hardware and typical operating pressures.

	Source chamber	First differential pumping stage	Second differential pumping stage	Main chamber
Mechanical roughing pump	Alcatel 2063 CP/ Edwards EH500 Roots blower	Alcatel 2033 CP	Alcatel 2033 CP (shared with FDC)	Alcatel 2033 CP
Diffusion pump	CVC PVMS-1000	Varian VHS-6	Varian VHS-6	Varian VHS-10
Diffusion pump fluid	DC-705	DC-705	DC-705	Santovac-5
Trap	None	Water-cooled baffle	Liquid N ₂	Liquid N ₂
Gate valve	None	6 in. manual	6 in. pneumatic	10 in. pneumatic
Approximate pumping speed	5300 L/s	1000 L/s	1000 L/s	2600 L/s
Pressure gauge	Tubulated B-A, W filament	Tubulated B-A ThO ₂ filament	Tubulated B-A, ThO ₂ filament	Nude B-A, ThO ₂ filament
Pressure controller	Varian 842	Varian 842	Varian 844	Varian 845
Base pressure	1×10^{-8} Torr	3×10^{-8} Torr	5×10^{-9} Torr	8×10^{-11} Torr
Pressure with beam on	4.5×10^{-4} Torr	2.5×10^{-5} Torr	9.1×10^{-7} Torr	1.7×10^{-7} Torr

molecular beamline. Table I details the vacuum hardware and operating pressures for each of the four chambers.

The chamber is constructed in three sections: the source, the first differential pumping stage, and the second differential pumping stage/main chamber. Mating surfaces joining the sections are precision machined to be flat and perpendicular to the beamline. Locating steps on the mating flanges and on the collimating orifices are machined to a tolerance of 25 μm and centered to within 25 μm of the beamline. This design ensures that the collimating orifices separating the four chambers remain precisely aligned, even after repeated separation and assembly of the chamber.

Molecules of interest expand into the source chamber from a 25 μm orifice in an Inconel 600 nozzle. Resistive heating allows the nozzle temperature to be varied from room temperature to 850 K with a stability of ± 0.5 K. Backing pressures for the methane/hydrogen mixtures in our current studies are typically 370 kPa. Reagent gases are handled in a bakeable stainless steel manifold evacuated by a liquid-nitrogen trapped diffusion pump. Seeding techniques vary the translational energy of the methane molecules over a chemically significant range from 5 to 100 kJ/mole. The supersonic beam exits the source chamber via a 1.04 mm diameter skimmer (Beam Dynamics, Model 1) located 9.40 mm downstream from the nozzle orifice.

After passing through the skimmer, the molecular beam enters the first differential pumping chamber and passes through an optical multipass cell¹⁷ where we excite a fraction of the molecules with infrared light. The cell's orthogonal excitation geometry collapses the inhomogeneous Doppler-broadened absorption profile and maximizes the number of molecules in the beam that are resonant with the infrared light. We use four uncoated Au mirrors, each 5 cm \times 1.5 cm, affixed to kinematic mounts and arranged in a diamond pattern. Dowel pins and precision locating holes reproducibly position the multipass cell assembly on the face of the chamber wall separating the source and first differential stages. A

sapphire window in the first stage admits infrared light into the chamber. The cell permits up to ten passes of the laser light through the molecular beam.

The first differential stage also houses an electromechanical shutter (Vincent Associates VS25S1T1). A timer of our own design allows for precisely timed doses ranging from 10 ms to 999 min. A machined skimmer with a clear aperture of 4.24 mm is located on the wall separating the first and second differential pumping stages and further collimates the beam.

A 152.4 mm diameter chopping wheel mounted on the shaft of a Globe Motor Model 75A1004-2 ac synchronous three-phase motor intercepts the beam after it enters the second differential pumping stage. A home-built motor driver, whose drive signal frequency is derived from a highly stable quartz crystal oscillator, powers the motor. The chopping wheel has four slots located 90° apart. Two 5.08 mm wide slots are centered at 0° and 180° on the wheel, and two 1.27 mm wide slots are centered at 90° and 270°. At its highest rate of revolution (400 Hz), the small slots in the wheel provide a gating function of 7.2 μs duration. For experiments with an unmodulated beam, a rack and gear mechanism positions the chopper wheel so the molecular beam passes unimpeded through the large slot.

A quadrupole mass spectrometer (QMS) housed in the main chamber is centered on the molecular beam axis. This QMS, in conjunction with a multichannel scaler (EG&G MCS-Plus) allows us to obtain time-of-flight spectra and measure directly the translational energy of the molecules incident on the surface. An integrated light emitting diode (LED)/photodiode sensor (QT Optoelectronics H22LOB) in the second differential chamber is positioned so that the large chopper wheel slot is centered over the sensor at the same time that the small slot is centered on the molecular beam. The photosensor generates a start pulse whenever the leading edge of the large slot passes the sensor. Since the edges of the large and small slots differ in their distance from the slot

TABLE II. Molecular beam size.

Beam valve aperture size	Beam size at Ni(100) crystal	Beam size at QMS ionizer
Small 2.01 mm	2.90 mm	4.70 mm
Medium 4.85 mm	6.99 mm	11.4 mm
Large 7.67 mm	11.0 mm	17.9 mm

center, the edge of the large slot passes the sensor before the edge of the small slot passes the molecular beam. For a typical chopper speed of 300 Hz, this effect causes the electronic start pulse to precede the leading edge of the gas pulse. We calculate a time shift of 14.5 μ s based on the tangential velocity of the slot at the molecular beam and the difference in edge-to-center distances for the large and small slots.

The second stage also houses a room-temperature pyroelectric detector with an integral source follower (Eltec 406-0). The detector is mounted on a linear motion feedthrough and can be translated into the beam path to monitor absorption of infrared light, or retracted to allow the molecular beam to pass through the second stage. Its use will be discussed further in Sec. III.

A sliding beam valve isolates the second differential chamber from the ultrahigh vacuum surface analysis chamber. The valve contains three orifices and an O-ring sealing mechanism. Translating the beam valve with a linear motion feedthrough allows us to define the beam's size or isolate the molecular beam source and surface analysis chambers. Table II summarizes the molecular beam size with each of the three apertures, both at the sample surface and at the entrance to the mass spectrometer ionizer assembly. The smallest aperture produces a beam image that passes freely through the quadrupole mass spectrometer's ionizer assembly and is best suited for time-of-flight measurements of the molecular beam. The medium aperture produces a beam image that is slightly smaller than the nickel crystal diameter. It ensures that molecules in the beam impinge only on the well-characterized face of the crystal and not on the crystal edge or the support assembly. When the large aperture is used, the skimmer separating the first and second differential chambers becomes the limiting orifice. The beam slightly overfills the crystal, ensuring that the entire crystal face is uniformly exposed to the beam.

After passing through one of the beam valve apertures, the molecular beam enters the main surface analysis chamber. This chamber houses the surface under study, an ion gun for sample cleaning, an Auger electron spectrometer for verifying surface cleanliness and quantifying reaction products, and a mass spectrometer for residual gas analysis, molecular beam characterization, and temperature programmed desorption measurements. The main chamber also has two bakeable, variable leak valves (Varian 951-5106) to admit gases required for crystal cleaning, dosing, or molecular beam flux calibration. A more detailed description of the chamber's contents follows.

A 1 cm diameter nickel single crystal oriented to within 0.1° of the (100) face (FOM Surface Preparation Laboratory) is mounted on the end of a cold finger (McAllister Technical Services LN2-Hat) by means of a custom-built OFHC cop-

per crystal support. Sapphire spacers electrically isolate the nickel crystal and its support from the manipulator, but provide thermal contact with the end of the cold finger assembly. The cold finger and crystal support are mounted on a manipulator (McAllister Technical Services MA2006) with 15.24 cm of vertical (z) translation and ± 1.27 cm of motion in the x and y directions. A doubly differentially pumped rotary feedthrough (McAllister DPRF) provides 360° of rotation about an axis passing through the face of the nickel crystal. A mechanical pump evacuates the outer seal of the rotary feedthrough while a 20 L/s ion pump (Varian 911-5030) evacuates the inner seal. Rotating the sample relative to the beam axis varies the angle of incidence of molecules impinging on the surface. Addition of liquid nitrogen to the cryostat cools the crystal to 78 K, or dry ice pellets in the cold finger cool the crystal to 196 K. A home-built proportional-integral-derivative (PID) temperature controller regulates current through a thoriated tungsten filament mounted behind the crystal and controls the surface temperature to within ± 0.5 K. Electron bombardment heating with a 200 V positive bias on the crystal raises the crystal temperature to high temperatures (up to 1100 K) for cleaning and annealing. The rear filament can also be used to heat the nickel crystal radiatively. A chromel-constantan (Type E) thermocouple spot welded to the edge of the crystal measures the crystal temperature. An Analog Devices 2B50A thermocouple signal conditioner provides an electronic ice-point reference, amplifies the thermocouple signal, and electrically isolates the crystal from our data acquisition electronics. Calibration of the thermocouple and detection electronics with liquid nitrogen, an ice bath, and boiling deionized water confirms that temperature readings are accurate to better than 1 K over this temperature range.

We clean the nickel surface with a combination of ion sputtering, oxidation, reduction, and annealing. An ion sputter gun (Phi 04-191), whose axis lies 68° off the surface normal, produces 500 eV argon ions. We adjust the background pressure of argon in the chamber to provide an ion current density of 2 μ A/cm² at the crystal surface. Argon ion sputtering for 3 min is generally sufficient to remove sulfur contamination from the nickel surface. Annealing the crystal for 15 min at 1100 K restores surface order. We then expose the crystal at room temperature to 1×10^{-7} Torr of O₂ for 50 s, followed by annealing at 875 K to oxidize and remove carbon contamination. Reduction in 1×10^{-6} Torr of H₂ for 4 min at 1000 K removes surface-bound oxygen. These cycles are repeated as necessary to produce a clean surface as determined by Auger electron spectroscopy.

An electron gun-hemispherical electron energy analyzer combination (VG Microtech LEG-63/VG-100AX), makes Auger electron spectroscopy measurements. The included angle between the electron gun and the electron energy analyzer is 60°, and we position the crystal so that its surface normal is oriented toward the electron energy analyzer. Three Helmholtz coils null magnetic fields in the vicinity of the sample. A channel electron multiplier/preamplifier/discriminator combination counts electrons passing through the hemispherical analyzer. Setting the electron gun emission to 10 μ A yields a 20 nA electron beam with a 1-mm-

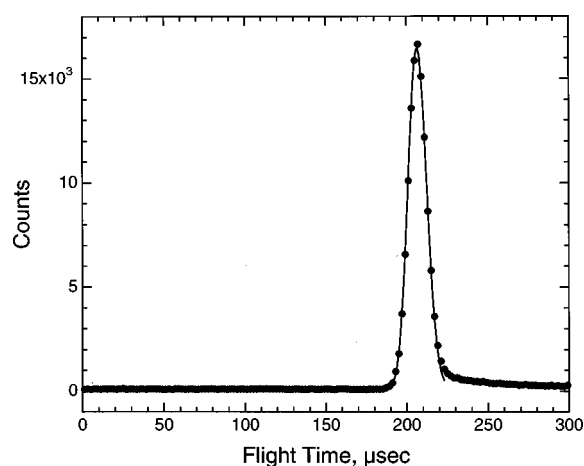


FIG. 3. Example of a time-of-flight spectrum for 2% CH_4 in H_2 expanding from a 400 K nozzle source. The points are the experimentally measured data and the solid line is a fit to the data. The translational energy is 63.4 kJ/mol and the translational temperature is 10 K.

diameter spot at the crystal and results in a 1.5 MHz count rate at the 848 eV Ni LMM peak. Section V details our use of the spectrometer to quantify reaction products.

A quadrupole mass spectrometer (UTI-100C) located on the beam axis performs residual gas analysis, temperature programmed desorption measurements, molecular beam characterization, and beam flux measurement. We have modified the mass spectrometer to permit pulse-counting detection of ions. A Philips Scientific Model 6908 preamplifier/discriminator converts detector pulses into TTL pulses for our prescaler and computer-based counter board.¹⁸

B. Molecular beam characterization

Time-of-flight (TOF) measurements characterize the distribution of velocities in our supersonic molecular beam.¹⁹ Figure 2 shows that the distance between the chopper and the center of the mass spectrometer ionizer is 50.01 cm. We record time-of-flight spectra with our multichannel scaler using a 2 μs dwell time per channel. We sum 10 000 or more passes to obtain a high signal-to-noise ratio and operate our mass spectrometer with an electron energy of 70 eV, an ion energy of 15 eV, and an emission current of 1 mA. Figure 3 shows a typical spectrum for a 2% methane in hydrogen gas mixture expanding from a 400 K nozzle source. We correct the flight-time spectrum for the mass-dependent ion flight time and the 14.5 μs lead time associated with our photosensor-generated start pulse to obtain a true flight time from chopper to ionizer. A nonlinear least-squares algorithm fits the flight time distribution to Eq. (1) of Ref. 20, with the modification that we numerically convolute that flight time distribution, which applies to a delta function in chopping, with the modulation function for our chopper wheel at the appropriate chopper speed. We have tested our analysis procedure on an Ar expansion from a room temperature nozzle and find that the argon achieves over 99% of the translational energy predicted for an ideal expansion. The solid line passing through the data in Fig. 3 is the result of such a fit for a seeded beam of methane in hydrogen. We find that our methane beams are also nearly ideal in their expansion and that

they have very narrow translational energy distributions ($\Delta E/E$ of less than 5% after deconvolution of the beam modulation function). This narrow distribution results in our experimentally determined sticking probabilities being averaged over a very narrow range of translational energies.

Many of the activated dissociative chemisorption reactions we study have reaction probabilities ranging from 10^{-3} to 10^{-6} . These low reaction probabilities preclude our using the method of King and Wells²¹ for measuring reaction probabilities. Instead, we obtain absolute reaction probabilities by dividing the surface coverage of reaction products by the integrated flux of reagents impinging on the surface during the dose. To obtain the flux of reagents in the molecular beam, we use our quadrupole mass spectrometer to measure the steady-state partial pressure of the reagent while the beam is running. We then multiply that pressure by the experimentally determined pumping speed for that species. We determine the flux in this way for each gas mixture, nozzle temperature, and backing pressure that we use.

To measure the steady-state partial pressure, we first direct the molecular beam onto the inert rear surface of our crystal mount and tune the QMS to monitor the species of interest. We record the ion count rate and close the beam valve to isolate the main chamber. We then leak in the pure gas of interest, with the mass spectrometer running, until we obtain an ion count rate identical to that with the molecular beam on. We turn off the mass spectrometer, record the pressure of the pure gas with the ionization gauge, and correct for relative ionization efficiencies to obtain the steady-state partial pressure.

We also use our mass spectrometer to measure the pumping speed for the reagent. We admit a continuous molecular beam to the chamber and monitor the partial pressure of the reagent with the QMS. We then interrupt the molecular beam with the beam shutter and follow the decay in the partial pressure of the species with our mass spectrometer and multichannel scaler. Fitting the decay to a single exponential decay yields a time constant for pumping the reagent. We multiply the reciprocal of this time constant by the experimentally determined volume of our chamber (85.4 L) to calculate the pumping speed. Our measured value of 2400 L/s for CH_4 is consistent with our predictions based on the specified pumping speed of the diffusion pump and the conductance of the gate valve and liquid nitrogen cold trap. Fluxes measured for our beams in this way range from $(2.5 \text{ to } 10.7) \times 10^{15}$ CH_4 molecules/($\text{cm}^2 \text{ s}$) at the surface, depending on the gas mixture and nozzle temperature.

III. OPTICAL EXCITATION AND INTERNAL ENERGY CONTROL

Infrared light from a high resolution, tunable laser crosses the molecular beam at a right angle and prepares an ensemble of excited molecules whose gas-surface reactivity may be studied.²² Two broadening mechanisms affect our ability to excite a known fraction of the molecules impinging on the crystal surface.¹⁶ Doppler broadening results in a shift in a molecule's absorption frequency that is proportional to its velocity component along the laser propagation direction.

We use an orthogonal excitation geometry so that the molecules' velocity along the flow axis does not contribute to Doppler broadening of the infrared transition. Still, the angular divergence of the molecular beam results in a small amount of Doppler broadening transverse to the molecular beam flow axis. This broadening is dramatically reduced relative to a room temperature sample, but it is significant compared to the 1 MHz bandwidth of our infrared laser. Doppler broadening is an inhomogeneous broadening mechanism; if we tuned our laser through an absorption profile dominated by Doppler broadening, different velocity subsets of molecules in the beam would be excited at each wavelength. A second broadening mechanism also affects the absorbers in our experiment. Molecules in the molecular beam travel at a high speed and pass through the laser excitation volume in a short time. The finite time each spends in the laser radiation field results in a homogeneous broadening of its absorption profile due to transit-time broadening. Doppler and transit-time broadening play an important role in our experiments. When we tune our laser to the center of the Doppler-broadened absorption profile, the laser can excite all molecules whose transverse velocities fall within a narrow range that is determined by the homogeneously broadened linewidth. Under the conditions of our experiment, this range of transverse velocities maps onto a spatially resolved stripe on our Ni(100) crystal surface. We plan to discuss this application of broadening mechanisms in laser-assisted surface chemistry in a subsequent publication.²³ For now, it is sufficient to note that all molecules in the correct ground rotational and vibrational state and impinging on the crystal center can be excited by the infrared laser.

The remainder of this section describes the experimental hardware we use to excite molecules in the beam and explains how we quantify the flux of vibrationally excited molecules impinging on the Ni(100) surface. The laser system that generates infrared light and the diagnostic hardware we use to characterize its operation are described in Sec. III A. In order to extract absolute, state-resolved reaction probabilities from our data, we must be sure that our optical pumping scheme excites a constant and reproducible fraction of molecules in the molecular beam for the entire duration of our measurement. We use several tools to verify and quantify infrared absorption by molecules in the molecular beam, and these tools are described in Sec. III B. Additional optical hardware and a computer-controlled feedback system are required to stabilize the laser's output wavelength and maintain a constant level of excitation throughout our measurement. Our system for actively stabilizing the laser output frequency is described in Sec. III C. We describe our procedure for determining the absolute flux of state-selected molecules impinging on the Ni(100) surface in Sec. III D.

A. Infrared laser and diagnostic hardware

An infrared laser provides quantum state selectivity in our experiments. A krypton ion laser (Coherent Innova 400-K3) operating on the 647.1 nm line excites a color center laser (Burleigh FCL-20). The color center laser is a continuous wave (cw) source of highly monochromatic infrared light continuously tunable from 2.3 to 3.3 μm . Its single

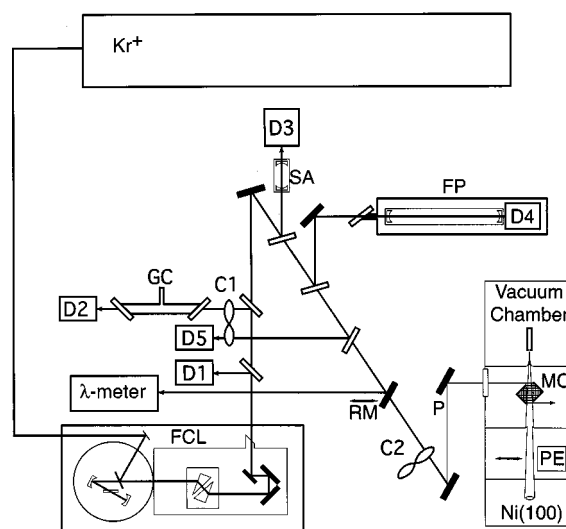


FIG. 4. Optical layout. Light from a Krypton ion laser (Kr^+) excites the gain medium in a color center laser (FCL). Mirrors (solid rectangles) redirect the beam, while beam splitters (open rectangles) typically reflect 1%–2% of the light to laser diagnostic equipment. A wave meter (λ meter), spectrum analyzer (SA), and vacuum-jacketed Fabry–Perot étalon (FP) characterize the infrared laser output. A removable mirror (RM) directs the infrared laser into the wave meter. D1 monitors the laser power at the dither frequency of the intracavity étalon, D2 monitors transmission through a room-temperature gas cell (GC), and D5 monitors laser power. Choppers (C1 and C2) modulate the beam for phase-sensitive detection. C2 intercepts the laser for absorption measurements in the molecular beam, but is removed when we pump molecules for surface reactivity measurements. A periscope, P , directs the beam into the molecular beam chamber and rotates the laser's polarization from horizontal to vertical. The light enters the multipass cell (MC), and a pyroelectric bolometer in the second stage (PE) monitors absorption in the molecular beam.

mode output has a spectral bandwidth of less than 1 MHz ($\Delta\nu/\nu \approx 10^{-8}$). For the studies of ν_3 excitation in methane discussed in Sec. V, we generate about 3 mW of infrared light at a wavelength of 3.29 μm . A portion of the infrared light is directed to diagnostic and frequency stabilization hardware, and the remainder is directed to the molecular beam chamber for state-selective excitation of the reagent molecules. Figure 4 shows the key features of the optical system.

Diagnostic equipment monitors laser performance and simplifies tuning the laser into resonance with the absorption transition of interest. A custom-built 7.5 GHz free spectral range spectrum analyzer monitors the laser mode structure and allows us to verify single mode output. A wavemeter (Burleigh WA-20IR) reads the vacuum wavenumber of the light to the nearest 0.01 cm^{-1} and guides our tuning of the laser. It also allows us to verify the identity of the transition we excite. A 150 MHz free spectral range Fabry–Perot étalon (Burleigh CFT-500IR) is temperature stabilized and housed in a vacuum jacket. It provides a high-resolution diagnostic of laser mode structure and also serves as a reference cavity for our frequency stabilization scheme. Commercially available (Burleigh RC-91) and home-built high voltage amplifiers and ramp generators²⁴ drive tuning elements in the spectrum analyzer, Fabry–Perot étalon, and the color center laser. A surface-absorbing calorimeter and read-

out unit (Scientech Models 36-0001 and 365, respectively) measure laser power.

B. Detecting infrared excitation

A small glass cell filled with a low pressure of the reagent gas (typically 1 Torr for methane) helps us quickly locate infrared transitions. An optical chopper (Palo Alto Research Model 300) modulates the portion of the laser light that is directed through the cell, and a PbSe detector, custom-built preamplifier, and lock-in amplifier (SRS Model 530) quantify transmission. The magnitude of the transmission signal near an absorption feature changes significantly if the color center laser suddenly shifts to a different longitudinal mode. It is a convenient diagnostic for identifying mode hops. As we tune the output of the color center laser, the gradient of the absorption signal indicates whether the laser is being tuned toward or away from the absorption maximum.

While the low-pressure absorption cell is helpful for locating infrared transitions, observing absorption in the cell does not ensure optical resonance with narrow absorption profile for molecules in the molecular beam. To ensure that we are exciting molecules in the molecular beam, we use a room-temperature pyroelectric detector inside the second differential pumping chamber to measure infrared absorption directly. When we wish to measure or verify absorption, we translate the detector into the beam, where molecules impinge on its surface.

The pyroelectric detector responds to temperature changes, and we exploit this feature to measure infrared absorption by molecules in the molecular beam. An unmodulated molecular beam impinging on the detector surface establishes a steady-state temperature that results in minimal detector signal. To detect infrared absorption, we modulate the infrared light at 4.1 Hz with a mechanical chopper (HMS 221). If the light is not resonant with an infrared absorption transition, the laser deposits no additional energy into the molecular beam. If molecules in the beam absorb light, a fraction of them can transfer their newly acquired internal energy to the detector, raise its temperature, and produce a detector response. A lock-in amplifier (SRS 530) monitors detector response at the laser modulation frequency and provides an output proportional to the absorption signal. Scanning the laser while monitoring the lock-in amplifier output results in an absorption spectrum of molecules in the beam. Figures 5(a) and 5(b) show signals from our low pressure absorption cell and the pyroelectric detector, respectively, as the laser is scanned through an absorption resonance with the R(1) transition to the ν_3 vibrational state in methane. Doppler broadening dominates the linewidth in room temperature cell, while both transit time and Doppler broadening contribute to the linewidth observed in the beam.

The 2 mm active area of the Eltec detector intercepts a solid angle of the molecular beam centered on the beam axis and smaller than that of the medium beam valve hole. Thus, the detector measures infrared absorption only for molecules that would impinge on the Ni(100) crystal were the detector removed from the beam path. Conversely, when we measure

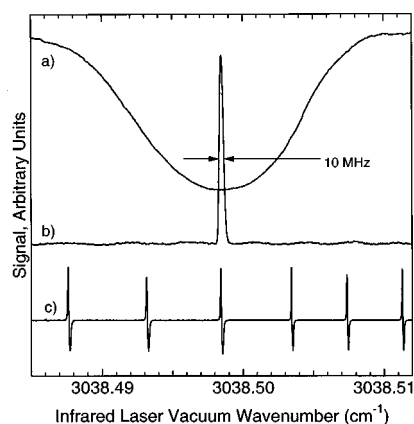


FIG. 5. Absorption spectrum of methane. (a) Absorption in room temperature cell; (b) absorption of molecules in molecular beam; (c) light transmitted through Fabry–Perot reference étalon.

absorption, we can be confident that upon translating the detector out of the beam path, a flux of state-selected molecules will impinge on the surface under study.

C. Laser frequency stabilization

The narrow bandwidth of the laser system and the narrow absorption profile of the molecules in the beam permit selective and efficient excitation of molecules in the beam, but they also present experimental challenges. Without active stabilization, the frequency of the infrared light will quickly drift out of resonance with the sharp absorption transition in the molecular beam, resulting in no excitation at all. In order to maintain resonance with the absorption transition, we actively stabilize two tuning elements in the color center laser. The first, an intracavity étalon, suppresses spurious longitudinal modes in the laser cavity and helps maintain single mode output. Its spacing can drift, resulting in mode and power instability. The second, the laser cavity end mirror, determines cavity length and sets the output frequency of the laser. Temperature and pressure fluctuations can alter the cavity's optical path length and lead to output frequency drift. A computer-controlled servo loop continuously adjusts both of these tuning elements to maintain stable output frequency, mode structure, and power.²⁵

We lock the intracavity étalon to its transmission maximum. A simple op-amp circuit sums the output of a 12-bit computer-controlled D/A converter and a small sinusoidal dither voltage and drives the external input of the étalon's piezoelectric driver (Burleigh RC-91). A PbSe photoconductive detector with a home-built preamplifier monitors light output of the laser, and a lock-in amplifier (Stanford Research Systems 530) measures the derivative signal resulting from our modulation of the étalon spacing. A LabView-based computer program reads the lock-in amplifier output and updates the D/A converter output to keep the étalon centered at the zero crossing of the derivative signal (i.e., at the peak of its transmission).

In order to measure low reaction probabilities, many of our experiments require the infrared laser to remain in resonance with the reagent's absorption feature for an hour or longer. Verifying infrared absorption with our pyroelectric

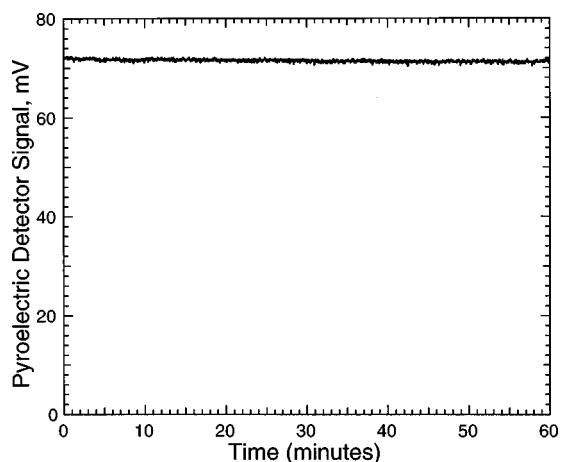


FIG. 6. Performance of the frequency stabilization system. The pyroelectric detector signal is shown as a function of time while the system is locked to the R(1) transition to ν_3 , $\nu=1$.

detector blocks the molecular beam from entering the ultra-high vacuum chamber and precludes our monitoring absorption during a dose. Instead, we lock the laser frequency to a vacuum jacketed and temperature stabilized Fabry–Perot étalon that we use as a frequency reference. We tune the laser into resonance with the absorption transition of interest and then adjust the Fabry–Perot cavity length to produce a transmission fringe at the frequency of the transition. We then apply a small (<1 MHz) dither to the output frequency using the cavity end mirror’s piezoelectric tuning element and monitor the derivative signal for transmission through the Fabry–Perot cavity with a lock-in amplifier. A computer-controlled servo loop analogous to that used to track the laser’s intracavity étalon monitors the lock-in amplifier output and tunes the cavity end mirror to maintain optimum transmission through the Fabry–Perot reference cavity. Figure 5(c) shows the derivative of the Fabry–Perot transmission signal for a typical scan. Note that the Fabry–Perot cavity length has been adjusted so that the zero crossing of one of the transmission fringes corresponds to the maximum of the infrared absorption signal.

This procedure results in excellent long-term stability. Figure 6 is a plot of methane absorption signal for the R(1) transition to the ν_3 C–H stretching state, measured with our pyroelectric detector, as a function of time. The rms fluctuations in the absorption signal, which arise from frequency and amplitude drift as well as nozzle backing pressure fluctuations, are less than 0.3% of the absorption signal over a period of 60 min. In addition, the excitation efficiency decreases by only 1% during the same time interval. This performance ensures that flux of vibrationally excited molecules remains constant during our measurements of their reactivity.

D. Quantifying excitation efficiency

To quantify reaction probabilities for state-selected molecules, we must know the absolute flux of state selected molecules impinging on the surface. We obtain that quantity in three steps. Since the infrared transition excites molecules from a single rotational and vibrational ground state (ν'', J'')

to the selected excited state (ν', J'), we first calculate the fraction of molecules in the molecular beam that are in the (ν'', J'') quantum state. Next, we calculate the fraction of those molecules that are excited by the infrared light. Finally, we multiply the product of those two fractions by the total flux of reagent molecules to obtain the absolute flux of state-selected molecules impinging on the surface. Section II B describes our procedure for measuring the total flux, and this section describes how we determine the fraction of molecules excited.

We measure the fraction of ground state (ν'', J'') molecules excited by infrared light, and then corroborate our measurement with two independent calculations of excitation efficiency. For our measurement, we rely on the nonlinear increase in infrared absorption as a function of laser power. Fitting this dependence to its known functional form results in an absolute measure of excitation efficiency. We calculate absolute excitation efficiencies using literature values for the infrared transition moment and our measured laser beam power, bandwidth, and spot size. Finally, we use the known pyroelectric detector and preamplifier sensitivity to calculate the amount of energy transferred to the detector by the laser-excited molecules. The energy accommodation coefficient for transferring a high-energy vibrational quantum in the incident molecule to the room temperature detector is not known. In the absence of a quantitative measure of energy accommodation, this final approach provides a relative estimate of excitation efficiency.

For all transitions we excite, the number of photons crossing the molecular beam exceeds the number of potential absorbers in the beam by a factor of 20 or more. Under these conditions, optical excitation can deplete the population in the transition ground state sufficiently to cause absorption to deviate from a linear function of incident laser power. Equation (1) predicts the fraction, f_2 , of the molecules in (ν', J') excited to (ν', J') by the infrared light:¹³

$$f_2 = \frac{g_2}{g_1 + g_2} \left\{ 1 - \exp \left[-\rho B_{21} \left(\frac{g_1 + g_2}{g_1} \right) t \right] \right\}. \quad (1)$$

Here, g_1 and g_2 are the degeneracies of the ground and excited states, respectively, ρ is radiation density at the transition frequency, B_{21} is the Einstein B coefficient for stimulated emission, and t is the time that the molecule spends in the coherent radiation field. In our experiment, t is the transit time for molecules in the molecular beam to fly through the laser excitation volume. If the laser radiation is not perfectly collimated, t must be modified to account for the curvature of the constant phase fronts in the laser radiation field. Thus, t depends on the kinetic energy of the absorbers in the beam and on the extent of collimation of the laser beam.¹⁶

Since all quantities in Eq. (1) are known, or can be experimentally measured, we can calculate f_2 for a given infrared transition. Herzberg gives degeneracies for a spherical top molecule,²⁶ and we calculate B_{21} from the squared, weighted transition moments, \mathfrak{A}_{12} tabulated in the HITRAN database.²⁷ Equation (2) gives B_{21} in $\text{m}^3/(\text{J s}^2)$ when \mathfrak{A}_{12} is in D^2 and Planck’s constant, h , has units of (J s):

$$B_{21} = \frac{8\pi^3}{3h^2} \frac{g_1}{g_2} \mathfrak{R}_{12} \times 10^{-49}. \quad (2)$$

For the $R(1)$ transition that we excite in Fig. 5, $\mathfrak{R}_{12} = 4.92 \times 10^{-3} D^2$ and $B_{21} = 5.6 \times 10^{16} \text{ m}^3/(\text{J s}^2)$. The radiation density, in units of $\text{J}/\text{m}^3 \text{ Hz}$, is given by Eq. (3), and depends on the laser power, P , the laser beam diameter, d , and the laser bandwidth, $\Delta\nu$:

$$\rho = \frac{4P}{\pi c d^2 \Delta\nu}. \quad (3)$$

For typical experimental conditions, we calculate a radiation density of $7.0 \times 10^{-12} \text{ J}/(\text{m}^3 \text{ Hz})$ based on 2 mW of laser power with an optical bandwidth of 1 MHz in a 1.1 mm diameter spot. For a perfectly collimated laser, t is the beam diameter divided by the molecular velocity. A beam of pure methane expanding from a room temperature nozzle has a velocity of about 1000 m/s, so $t = 1.1 \mu\text{s}$ for the limiting case of a collimated laser beam. For a diverging or converging laser beam, that quantity is modified by the multiplicative factor $1/[1 + (\pi w^2/R\lambda)^2]$, where R is the radius of curvature for the constant phase fronts of the laser radiation, w is the laser beam waist at the molecular beam crossing, and λ is the wavelength.¹⁶ We estimate that $R = 0.2 \text{ m}$, based on the location of the focal spot relative to the multipass cell, so a more accurate estimate yields $t = 0.45 \mu\text{s}$. For the transition depicted in Fig. 5, g_1 and g_2 are 3 and 5, respectively, so a single laser-molecular beam crossing excites 23% of the $v'' = 0, J'' = 1$ population to $v_3, v' = 1, J' = 2$. Additional laser-beam crossings in the multipass cell increase the experimentally realized excitation efficiency beyond this calculated value, although f_2 for subsequent passes is reduced sharply by divergence of the laser beam. While the exact values of the laser spot size and R may vary slightly from these values depending on the details of our optical layout, this calculation shows that we can excite a significant fraction of ground state molecules under typical experimental conditions.

Equation (1) also gives the expected functional dependence for absorption as a function of laser power. When the laser is tuned to the peak of a given transition, level degeneracies and B_{21} become constants, as do the transit time and laser spot size, as long as the expansion conditions for the molecular beam and focusing conditions for the laser remain unchanged. The only remaining parameter in Eq. (1), the radiation density, is linearly dependent on laser power through Eq. (3). A measurement of absorption signal as a function of laser power should follow the functional form of Eq. (1), asymptotically approaching the signal corresponding to $f_{2,\infty} = g_2/(g_1 + g_2)$ at high laser power. Figure 7(a) shows the results of a series of such measurements. Absorption is measured as mV of signal from our pyroelectric detector/preamplifier combination, and laser power is reported as mV of signal from a PbSe photoconductive detector and preamplifier. The solid lines passing through the data are fits to the functional form:

$$y = y_{\max} [1 - \exp(-A_1(P - A_2))], \quad (4)$$

where A_2 accounts for small voltage offsets in our laser power measurement electronics and y_{\max} is the pyroelectric

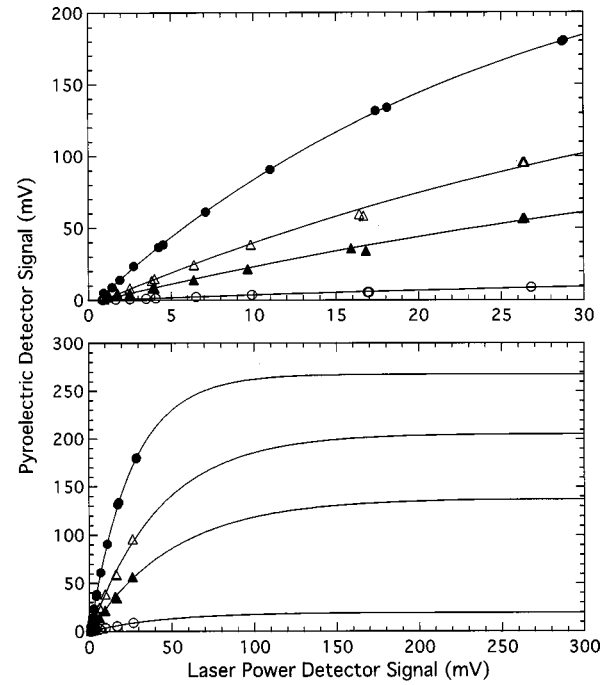


FIG. 7. Saturation behavior of the infrared absorption signal and theoretical fits to the data. (●): 100% CH_4 expanded from 291 K nozzle; (○): 100% CH_4 expanded from 751 K nozzle; (△): 25% CH_4 expanded from 289 K nozzle; (▲): 25% CH_4 expanded from 401 K nozzle.

signal we would measure if saturation were complete. We treat A_1 as an adjustable parameter in our fit of data for the pure methane beam expanding from a nozzle source at 291 K. That beam is the slowest of those we study, and, since it most nearly reaches saturation, it best constrains the A_1 parameter. A_1 varies linearly with transit time, so we adjust its value for differences in transit time and use it as a constrained parameter in our fits to other saturation data sets. Figure 7(b) shows the fits extrapolated to their asymptotic limit. The ratio of the maximum measured absorption signal to y_{\max} gives the fractional extent to which we saturate the transition, f_{sat} . The product of f_{sat} and the degeneracy factor $g_2/(g_1 + g_2)$ is f_2 , the fraction of (v'', J'') molecules excited from (v'', J'') to (v', J') .

When we vary the speed of molecules in the molecular beam, Eq. (1) predicts that f_2 will vary with transit time. We test the consistency of our data by measuring the transit-time dependence of our excitation fractions. We keep the maximum laser power, laser focal properties, and optical transition constant, but vary the speed of the methane molecules in the molecular beam by varying the nozzle source temperature and seeding conditions. We analyze each power-dependence curve as described above and obtain a value of f_2 for each set of beam conditions. Figure 8 shows these values of f_2 plotted versus transit time. We fit these data to the functional form:

$$y = f_{2,\infty} [1 - \exp(-A_3 t)]. \quad (5)$$

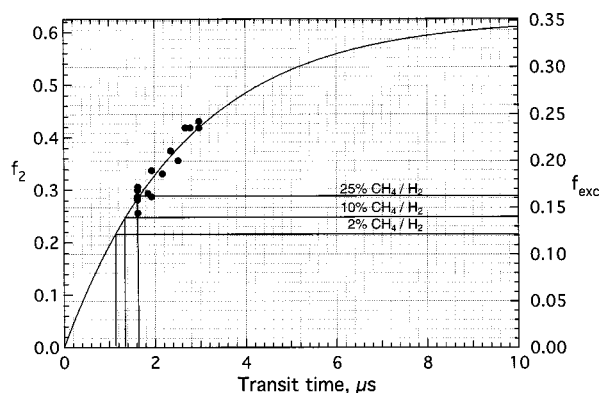


FIG. 8. Extent of saturation as a function of transit time. The right-hand side axis shows total excitation probability, assuming complete rotational relaxation into the lowest levels allowed by nuclear spin symmetries. Transit times and the corresponding excitation probabilities are shown for three gas mixtures expanding from a 400 K nozzle.

We constrain $f_{2,\infty} = 5/8$ for the $R(1)$ transition and treat A_3 as an adjustable parameter. The solid line passing through the data is the result of our fit.

In order to calculate the total fraction of the beam excited, we need only multiply f_2 by the fractional population of the (v'', J'') ground state. The ground vibrational state population exceeds 96% at a nozzle temperature of 400 K. Nuclear spin statistics in methane restrict the rotational relaxation of methane in a supersonic molecular beam. If rotational relaxation were complete, 9/16 of the population would relax into $J'' = 1$. In that case, the total fraction of all methane molecules in the beam that we excite for the $R(1)$ transition is

$$f_{\text{exc}} = f_{v=0} f_2 (9/16) \approx (9/16) f_2. \quad (6)$$

Figure 8 shows f_{exc} values on the right-hand side axis and illustrates how we obtain overall excitation fractions for several seeded molecular beams based on their measured velocities and calculated transit times. Our ability to measure infrared absorption for a variety of rovibrational transitions allows us to determine experimentally the extent of rotational relaxation in the molecular beam. In cases where rotational relaxation is not complete, we simply modify Eq. (6) to reflect the proper ground state fractional population. We use the fractional excitation measured in this way to calculate our state-resolved sticking probabilities.

Our room temperature pyroelectric detector provides a relative means of estimating excitation efficiency.²⁸ The detector has a responsivity of 3000 V/W at the 4.1 Hz modulation frequency of the infrared light. The responsivity, when coupled with the $200\times$ gain of our preamplifier, yields an instrument response of 6×10^5 V/W. When exciting the $R(1)$ transition to v_3 in a pure methane beam expanded from a room temperature nozzle source, we observe a detector signal of 200 mV. This signal corresponds to 3×10^{-7} W of power deposited at the detector by the laser-excited methane molecules and would arise if 5×10^{12} vibrationally excited molecules deposited all of their internal energy at the detector each second. Given the flux of the pure methane beam, the location of the pyroelectric detector along the beamline, and the 2 mm diameter detector area, 1.3×10^{15} CH_4 mol-

ecules impinge on the detector each second. If energy accommodation were complete, our detector signal indicates that we excite 0.4% of all methane molecules in the beam. This estimate should be viewed as a very conservative lower bound on the fraction of molecules excited, since energy accommodation is unlikely to be complete. Faubel and Schlemmer reported excellent agreement between experiment and predictions of energy accommodation of a methane beam on a similar room temperature detector by entirely neglecting the vibrational contribution to methane's heat capacity.²⁹ Their result is in accord with the general observation that vibrational energy is typically much less easily transferred upon collision than is rotational or translational energy. Thus, we expect that accommodation of the high-frequency C–H stretching quantum on the lithium tantalate detector surface is rather inefficient. We note that an accommodation coefficient of 0.016 for vibrational energy would bring our estimation of excitation efficiency from our pyroelectric detector into quantitative agreement with the results summarized in Fig. 8.

IV. REACTION PRODUCT DETECTION

We obtain absolute sticking probabilities by dividing the number of reaction products, as determined by Auger electron spectroscopy, by the integrated flux of reactants impinging on the surface. For our studies of methane dissociation, we hold the surface temperature at 475 K during the dose to promote the rapid recombinative desorption of the hydrogen carrier gas in our molecular beam. At that surface temperature, molecularly adsorbed CH_4 desorbs very rapidly, the methyl reaction product dehydrogenates and hydrogen atoms recombinatively desorb, but the carbon atom remains bound to the surface. Therefore, surface-bound carbon is a quantitative signature of methane's dissociative chemisorption. We adjust the molecular beam dose time to produce 0.08–0.10 ML of carbon on the surface and verify that adsorption is a linear function of exposure up to that coverage.

To calculate absolute reaction probabilities, we require absolute coverage measurements of the surface-bound reaction products. We use the integrated Auger electron peak for the Ni LMM line as an internal standard and the ratio of the carbon KLL to the Ni LMM peak integrals as a relative measure of carbon coverage. The known, self-limiting saturation coverage of ethylene on Ni(100) calibrates our AES measurements. Figure 9 shows the C/Ni ratios calculated for a series of ethylene doses as a function of dose time. The plateau at a C/Ni ratio of 0.12 corresponds to the 0.50 ML saturation coverage reported by Klink *et al.*³⁰ We calibrate our C/Ni ratios to this limiting coverage and report the corresponding fractional coverages on the right-hand side axis of Fig. 9. Based on carbon measurements at low coverages, we estimate our detection limit for carbon on Ni(100) to be 0.005 ML.

V. APPLICATION TO METHANE DISSOCIATIVE CHEMISORPTION ON Ni(100)

We illustrate the use of our apparatus with a state-resolved measurement of methane dissociation on Ni(100).

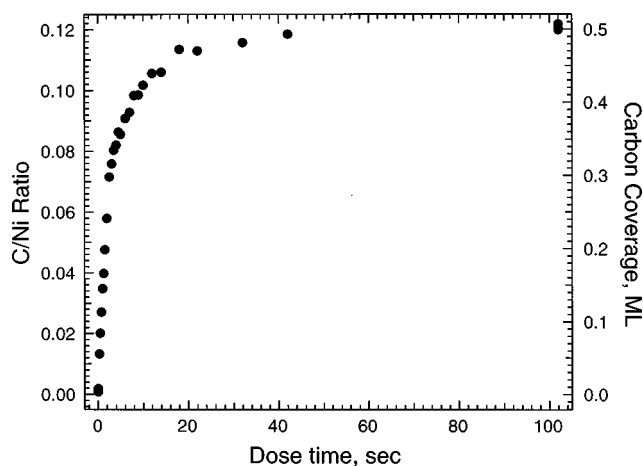


FIG. 9. Auger C/Ni ratio as a function of ethylene dose time. The corresponding carbon coverage, expressed in ML relative to the Ni surface atom density, appears on the right-hand side axis.

We begin by cleaning the Ni(100) crystal and verifying its cleanliness with AES. The time-of-flight measurement illustrated in Fig. 3 verifies that our 2% mixture of methane in hydrogen has a mean translational energy of 63.4 kJ/mole when expanded from a 400 K nozzle source. We tune our infrared laser into resonance with the peak of the methane transition from ($v''=0, J''=1$) to ($v'(\nu_3)=1, J'=2$), the $R(1)$ transition at 3038.4985 cm^{-1} . We use the pyroelectric detector in the beam path to locate the center of the transition, as illustrated in Fig. 5, adjust the Fabry–Perot étalon to a transmission maximum at that frequency, and lock the laser frequency to the reference cavity transmission maximum. We open the timed shutter and allow the molecular beam to impinge on the crystal face for 120 s. The crystal temperature controller maintains the surface temperature at 475 K throughout the dose. Once the dose is over, we rotate the crystal to face the hemispherical analyzer, turn on the 3 kV electron beam, and collect Auger electron spectra of the carbon KLL and nickel LMM lines. We integrate the peaks and obtain the fractional carbon coverage from the calibration curve in Fig. 9. We measure the total flux of the molecular beam, as described in Sec. II B. Next, we repeat the experiment, but without the laser on. This measurement provides an average sticking probability for the ensemble of thermally excited vibrational states in the molecular beam. We generally measure the sticking probability in this way at least three times for each set of experimental conditions, and average the sticking probabilities to reduce the error in our measured quantities.

A previous publication describes our data analysis procedure.⁵ We have shown that the state-resolved sticking probability for the laser excited state is given by

$$S_0^{\nu_3} = \frac{S_0^{\text{laser on}} - S_0^{\text{laser off}}}{f_{\text{exc}}} + S_0^{\nu=0}, \quad (7)$$

where $S_0^{\text{laser off}}$ is the sticking probability measured with the laser off, $S_0^{\text{laser on}}$ is the sticking probability measured with the laser on, f_{exc} is the fraction of molecules excited by the laser (given by Fig. 8), and $S_0^{\nu=0}$ is the sticking probability for molecules in the vibrational ground state. Typically, $S_0^{\nu=0}$

is much less than the first term in Eq. (7), so it contributes minimally to the state-resolved sticking probability. For the conditions of our experiment, we measure $S_0^{\text{laser on}} = 8.4 \times 10^{-4}$, $S_0^{\text{laser off}} = 1.7 \times 10^{-4}$, and $f_{\text{exc}} = 0.12$ and estimate $S_0^{\nu=0} \approx 7 \times 10^{-7}$ from the model of Holmblad *et al.*²⁰ We therefore calculate $S_0^{\nu_3}$ to be 5.8×10^{-3} for the ν_3 $v=1, J=2$ eigenstate at a translational energy of 63.4 kJ/mol.

VI. DISCUSSION

In summary, we have described a new experimental apparatus that combines supersonic molecular beams, ultrahigh vacuum surface science analytical tools, and optical pumping with a narrow bandwidth infrared laser to measure eigenstate-resolved sticking probabilities for dissociative chemisorption. A state-resolved measurement of methane dissociation on Ni(100) demonstrates our ability to perform these measurements. This combination of experimental tools provides the highest possible level of control over the internal quantum states of the reagents, and also a high level of control over the reagent's translational degrees of freedom. In addition, the temperature and chemical composition of the surface under study may be specified. The apparatus makes feasible a new generation of highly detailed experiments that can unambiguously reveal the key features that dominate the dynamics of gas-surface reactivity.

ACKNOWLEDGMENT

The authors gratefully acknowledge the support of this work by the National Science Foundation through Award No. CHE-9703392.

- ¹D. C. Jacobs, *J. Phys.: Condens. Matter* **7**, 1023 (1995).
- ²P. L. Houston and R. P. Merrill, *Chem. Rev.* **88**, 657 (1988).
- ³M. Gostein and G. O. Sitz, *J. Chem. Phys.* **106**, 7378 (1997).
- ⁴H. Hou, Y. Huang, S. J. Guiding, C. T. Rettner, D. J. Auerbach, and A. M. Wodtke, *Science* **284**, 1647 (1999).
- ⁵L. B. F. Juurlink, P. R. McCabe, R. R. Smith, C. L. DiCologero, and A. L. Utz, *Phys. Rev. Lett.* **83**, 868 (1999).
- ⁶C. T. Rettner, D. J. Auerbach, J. C. Tully, and A. W. Kleyn, *J. Phys. Chem.* **100**, 13021 (1996).
- ⁷C. T. Rettner, H. A. Michelsen, and D. J. Auerbach, *Chem. Phys.* **175**, 157 (1993).
- ⁸H. A. Michelsen, C. T. Rettner, D. J. Auerbach, and R. N. Zare, *J. Chem. Phys.* **98**, 8294 (1993).
- ⁹C. T. Rettner, D. J. Auerbach, and H. A. Michelsen, *Phys. Rev. Lett.* **68**, 1164 (1992).
- ¹⁰M. J. Cardillo, *Annu. Rev. Phys. Chem.* **32**, 331 (1981).
- ¹¹S. T. Ceyer, *Annu. Rev. Phys. Chem.* **39**, 479 (1988).
- ¹²C. T. Rettner and D. J. Auerbach, *J. Electron Spectrosc. Relat. Phenom.* **45**, 335 (1987).
- ¹³R. B. Bernstein, *Chemical Dynamics via Molecular Beam and Laser Techniques* (Oxford University Press, New York, 1982).
- ¹⁴G. Scoles, *Atomic and Molecular Beam Methods* (Oxford University Press, New York, 1988).
- ¹⁵P. Hess and C. B. Moore, *J. Chem. Phys.* **65**, 2339 (1976).
- ¹⁶W. Demtröder, *Laser Spectroscopy Basic Concepts and Instrumentation*, 2nd ed. (Springer, Berlin, 1996).
- ¹⁷T. E. Gough, D. Gravel, and R. E. Miller, *Rev. Sci. Instrum.* **52**, 802 (1981).
- ¹⁸P. R. McCabe and A. L. Utz, *Rev. Sci. Instrum.* **69**, 1909 (1998).
- ¹⁹D. J. Auerbach, in *Atomic and Molecular Beam Methods*, edited by G. Scoles (Oxford University Press, New York, 1988), Vol. 1, pp. 362–379.

- ²⁰P. M. Holmblad, J. Wambach, and I. Chorkendorff, *J. Chem. Phys.* **102**, 8255 (1995).
- ²¹D. A. King and M. G. Wells, *Proc. R. Soc. London, Ser. A* **339**, 245 (1974).
- ²²R. E. Miller, in *Atomic and Molecular Beam Methods*, edited by G. Scoles (Oxford University Press, New York, 1992), Vol. II, pp. 192–212.
- ²³L. B. F. Juurlink and A. L. Utz (unpublished).
- ²⁴P. Horowitz and W. Hill, *The Art of Electronics*, 2nd ed. (Cambridge University Press, Cambridge, 1989).
- ²⁵J. V. V. Kasper, C. R. Pollock, R. F. Curl, Jr., and F. K. Tittel, *Appl. Opt.* **21**, 236 (1982).
- ²⁶G. Herzberg, *Molecular Spectra and Molecular Structure II. Infrared and Raman Spectra of Polyatomic Molecules* (Van Nostrand Reinhold, New York, 1945).
- ²⁷L. S. Rothman, C. P. Rinsland, A. Goldman, S. T. Massie, D. P. Edwards, J. M. Flaud, A. Perrin, C. Camy-Peyret, V. Dana, J. Y. Mandin, J. Schroeder, A. McCann, R. R. Gamache, R. B. Wattson, K. Yoshino, K. V. Chance, K. W. Jucks, L. R. Brown, V. Nemtchinov, and P. Varanasi, *J. Quant. Spectrosc. Radiat. Transf.* **60**, 665 (1998).
- ²⁸R. E. Miller, *Rev. Sci. Instrum.* **53**, 1719 (1982).
- ²⁹M. Faubel and S. Schlemmer, *J. Phys. E* **21**, 75 (1988).
- ³⁰C. Klink, L. Olesen, F. Besenbacher, I. Stensgaard, E. Laegsgaard, and N. D. Lang, *Phys. Rev. Lett.* **71**, 4350 (1993).